4 EARLY PATTERNS IN WOUND HEALING

Abstract

The mechanisms by which cells move in a coordinated fashion have been studied intensively for decades. Current wound healing studies focus primarily on how cells migrate collectively within the cell sheet. However, how cells generate patterns and select one wound healing mechanism over the other has yet to be explored. The wound healing behavior of Madin-Darby Canine Kidney (MDCK) epithelial cells was examined *in vitro*, using circular wounds of increasing diameters. A unique wound healing pattern was observed on aECM surfaces: "leader cell groups" formed along the wound edge, separated by regions of actomyosin "purse strings". This unique healing pattern was observed only on aECM surfaces, and not on glass. The spacing between consecutive leader cell groups was found to be independent of wound diameter. However, this spacing decreased with increasing concentrations of blebbistatin, a myosin II inhibitor. The wound healing behavior could be explained by a simple force transmission model. We verified experimentally that the selection of wound mechanism could be controlled by wound geometry. These results are consistent with the model predictions.

4.1 Introduction

How cells move together to heal a wound is fundamentally relevant to tissue repair, tumor progression, and developmental biology. Recent experiments have identified two distinct healing mechanisms (*1*). First, wound closure can occur via a "purse string" mechanism where cells use the motor protein myosin II to assemble actin filaments into a contractile bundle along the wound edge (*2-3*). The bundle contracts and generates mechanical forces, which can be transmitted continuously through intercellular adhesions along the wound edge (*3-5*). This draws the cell sheet into the wound area, thereby closing the gap (*6-7*). The second mechanism requires cells at the wound edge to extend their lamellipodia and pull the cells behind them as they migrate in the direction of the wound. Morphologically, they resemble "finger-like" protrusions and have been termed "leader cells" (*8-9*).

Current studies on wound healing have primarily focused on how cells create collective migration within the cell sheet (*9-10*). However, how cells select one mechanism over the other is still unclear. In this work, we attempted to address how cells select one healing mechanism over the other along the periphery of the wound.

We use an *in vitro* "barrier" wound healing assay, similar to that described in earlier chapters. To study wounds of controlled geometries and diameters, we used microfabrication to create micropatterned PDMS blocks to be used as barriers in the assay. The Madin-Darby Canine Kidney (MDCK) cell model was used because the MDCK cells display collective behavior and has shown both purse-string and lamellipodial crawling mechanisms in *in vitro* healing assays (*11*). We also examined

how MDCK cells responded to artificial extracellular matrix (aECM) proteins containing the full-length fibronectin 10 cell binding domain (Figure 4.1). This aECM protein has been shown to promote wound healing, similar to fibronectin *in vitro* in Chapter 3.

M MASMTGGQQMG HHHHHHH DDDDKLD[(VPGIG)$_2$VPGKG(VPGIG)$_2$]$_6$FN10m[(VPGIG)$_2$VPGKG(VPGIG)$_2$]$_6$LE

FN10m:
VSDVPRDLEVVAATPTSLLISWDAPAVTVRYYRITYGETGGNSPVQEFTVPGSASTATISGLAPGVDYTITV YAVTGRGDSPASSAPISINYR

Figure 4.1 Amino acid sequence of aECM protein containing the fibronectin 10 domain

4.2 Materials and methods

Reagents

All reagents were purchased from Sigma-Aldrich unless otherwise specified. Phalloidin-rhodamine, mouse anti-T7 tag primary antibody, and goat anti-mouse FITC secondary antibody were obtained from Chemicon. The SU-8 3050 photoresist was obtained from MicroChem Corp (Newton, MA), silicon wafers were purchased from Wafer World, Inc. (West Palm Beach, FL), and polydimethylsiloxane (PDMS, Sylgard® 184) was from Dow Corning (Midland, MI). The tridecafluoro-1,1,2,2-tetrahydrooctyl-1-trichlorosilane was purchased from United Chemical Technologies, Inc. (Bristol, PA). Bis(sulfosuccinimidyl) suberate (BS^3) was from Pierce (Rockford, IL). All cell culture reagents were obtained from Invitrogen (Carlsbad, CA). Fibronectin solution was from Chemicon.

Preparation of aECM substrates

Glass coverslips (No. 1, round, 25 mm diameter) were cleaned in KOH/ethanol solution for 30 min and incubated in 6N NaOH for 10 min. The treated coverslips were washed briefly in distilled H_2O and incubated in 2% 3-aminopropyltriethoxysilane/95% ethanol/H_2O solution for 2 min at room temperature. Subsequently, amine-functionalized glass coverslips were rinsed with methanol for 2 min and air-dried. The aECM protein containing the full-length FN10 domain was cloned, expressed, and purified as previously reported (see Figure 4.1). The aECM protein was dissolved in distilled H_2O (25 mg/ml) and crosslinked with bis(sulfosuccinimidyl) suberate (BS^3, 100 mg/ml in distilled H_2O) at 4 ºC. The protein mixture was pipetted onto amine-functionalized glass coverslips and spin-coated at 5000 rpm for 30 s at 4 ºC. aECM protein films were dried overnight at 4 ºC before use.

Cell culture

MDCK cells were generous gifts from Elowitz laboratory (Caltech). Cells were maintained in Dulbecco's modified eagle medium (DMEM) containing 10% fetal bovine serum, 1% penicillin/streptomycin, and phenol-red (growth medium). Cells from passages 10 to 30 were used with no observable differences in growth and cell morphologies. All experiments were performed in DMEM lacking phenol-red, supplemented with 1% penicillin/streptomycin (serum-free medium).

Microfabrication of micropatterned PDMS blocks

The wound features were designed using DesignCAD software and printed on transparencies as positive photomasks (CAD/Art Services, Inc., Bandon, OR) as shown in Figure 4.2. Standard photolithography techniques were used to fabricate mold features that were 50 μm high (*12*). Briefly, the SU-8 3050 photoresist was spin-coated on a silicon wafer at 3000 rpm, exposed to UV light through a photomask, and developed to form a "master" mold. We pre-coated the master with tridecafluoro-1,1,2,2-tetrahydrooctyl-1-trichlorosilane for 30 min under vacuum to facilitate subsequent removal of the cured PDMS. PDMS was mixed at 10:1 PDMS base/curing agent ratio, degassed for 15 min, poured over the master, and cured overnight at 80 ºC. PDMS was peeled from the master, and cut into blocks for subsequent wound healing experiments. A sharpened blunt-end needle was used to punch holes through the blocks to allow injection of cells and media underneath the block.

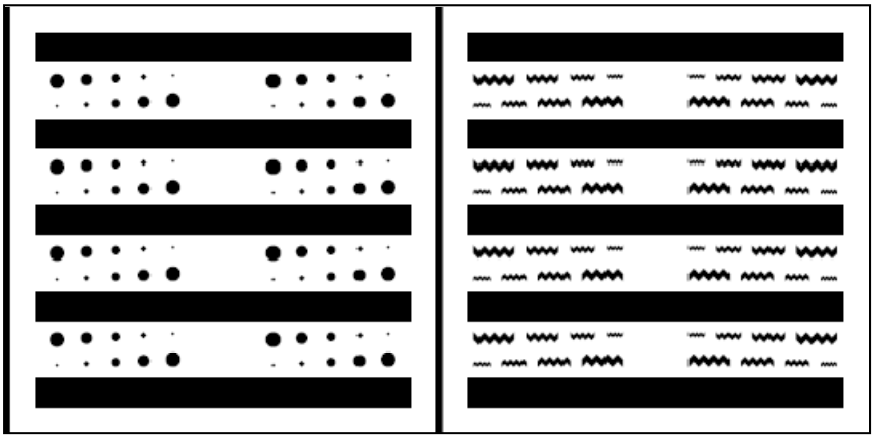

Figure 4.2 Design of micropatterned PDMS blocks for creating circular and zigzag-shaped wounds

Wound healing

The wound healing assay used in this chapter was modified from previous work (see Chapter 2, Figure 2.2A). PDMS blocks bearing the wound features (microposts) were cleaned with ethanol, air-dried, inverted, and pressed firmly onto a clean petri dish surface. To prevent non-specific adhesion of cells to the PDMS micropatterns, we pre-coated the walls of each PDMS block with 1 % Pluronic F-127 for 10 min at room temperature. The Pluronic was aspirated with a vacuum pump and the blocks were quickly dried with a jet of sterile air. At the same time, untreated glass coverslips or glass coverslips containing the spin-coated aECM films were mounted in 6-well tissue culture plates (BD Biosciences, CA) using silicone glue (GE healthcare, Piscataway, NJ). The Pluronic-treated PDMS blocks were pressed firmly onto the center of each coverslip. To allow cells to adhere to glass, fibronectin solution (10 μg/ml in PBS) was incubated underneath the blocks overnight at 4 ºC. The next day, MDCK cells were injected underneath the PDMS blocks and allowed to grow to confluence around the micropatterns. The PDMS blocks were subsequently removed, creating a wound of controlled shape. The wound healing process was observed using time lapse phase contrast microscopy (Figure 4.3).

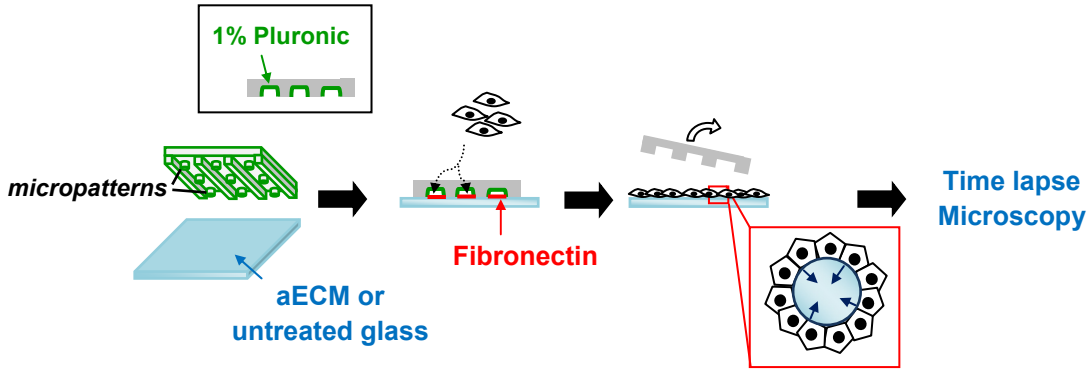

Figure 4.3 Schematic of wound healing assay. PDMS blocks were pre-treated with 1% pluronic and placed on either aECM or untreated glass substrates. Fibronectin was adsorbed underneath the stamps to aid cell adhesion. When MDCK cells were grown to confluence, the PDMS stamps were removed, revealing circular wounds previously occupied by the micro wound features. Wounded cell sheets were then observed using time lapse microscopy until wound closure.

Fluorescence imaging

The MDCK cell monolayers were wounded as described in Figure 4.3 and maintained in serum-free medium at 37 ºC for 4 h. Cells were fixed with pre-warmed 3.7% paraformaldehyde in PBS at pH 7.5 for 20 min at 37 ºC. After washing with PBS, cells were blocked in blocking solution (10% FCS, 5% sucrose, 2% BSA in PBS) for 30 min at room temperature. To visualize actin, cells were incubated with 100 µl of rhodamine-phalloidin in 1 ml PBS (1:50 Molecular Probes, Inc., Eugene, OR) for 1 h at 37 ºC. In order to detect the aECM protein, wounded monolayers migrating on aECM protein substrates were fixed, blocked, and incubated with a primary mouse anti-T7 tag antibody (1: 1000) in PBS for 2.5 h at 37 ºC, followed by a secondary anti-mouse FITC

(1: 2000). Glass coverslips were mounted with 1:1 glycerol in PBS and imaged using an Zeiss Axiovert 200M microscope with epifluorescence optics and AxioVision LE software.

Myosin II inhibition studies

Cell monolayers were wounded and allowed to migrate on glass substrates in serum-free media containing various concentrations of (-) blebbistatin. Images of the wound area were acquired every 15 min for 24 h to obtain time-lapse videos.

Image analysis using MATLAB

To facilitate the analysis, we first outlined the wound edge using the properties of phase contrast and then identified leader cells by using the local geometry along the wound edge. The phase contrast effect enhanced the periphery of cell bodies along the wound edge. This allowed us to identify the edge of wound by comparing the intensity difference between neighboring pixels. The contour of the edge of the wound was iteratively smoothed using a nearest neighbor averaging method until the difference was less than a pre-set threshold. To identify the leader cell groups along the contour, we set three criteria. First, the leader cell group must be closer to the geometrical center of the wound than its neighboring points. Second, the local curvature around the leader cell group must be concave inward. Third, the migration of leader cell group must be moving toward the geometrical center of the wound. Once the leader cell groups were identified,

we tracked their speed of migration and separation distances along the edge of the wound. The number of leader cell groups and the spacing between them were calculated relative to the image at t = 0 h, and averaged for all frames. Since the program is limited to non-complicated contours, we limited our analysis to the first 4 h of each wound healing movie. Moreover, other factors such as cell-cell signaling have been shown to drive wound closure (*13-14*) at longer times (> 4 h).

4.3 Results and Discussion

We performed wound healing assays and allowed cell monolayers to migrate on aECM and glass substrates. To decouple from the effects of biochemical pathways, wound healing experiments were performed in the absence of serum and growth factors. In the same experiment, we also examined the effect of wound size by creating wounds of different diameters ranging from 300 to 500 μm. Under our wounding conditions, the aECM protein surface appeared intact after removal of the PDMS stamp. We further verified the integrity of the surface by labeling the N-terminal T7 tag of the aECM protein (Figure 4.4).

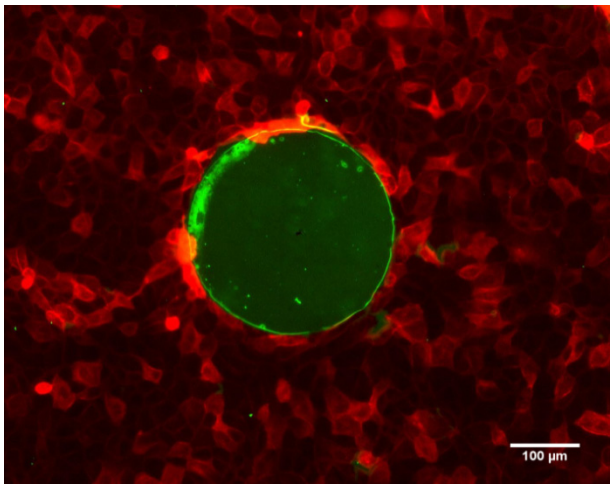

Figure 4.4 Removal of PDMS preserved aECM protein surface underneath. Cells were grown to confluence underneath the PDMS stamps. Following removal of the PDMS stamp, the cell sheets were immediately fixed and stained for F-actin (red) and the T7 tag (green). This confirmed that the original aECM protein substrate (green) was not affected by the PDMS micro wound features.

Wound closure on aECM protein substrates was generally complete by 10 h. On aECM surfaces, leader cells developed within 1 h after wounding, and these leader cells persisted until the entire wound area was closed (Fig 4.5, left panel). A striking pattern was observed on these substrates: leader cells appeared at regular intervals along the periphery of the wound. Figure 4.6A shows the presence of leader cells (white arrows) and purse strings (yellow triangles) in wounds stained for F-actin.

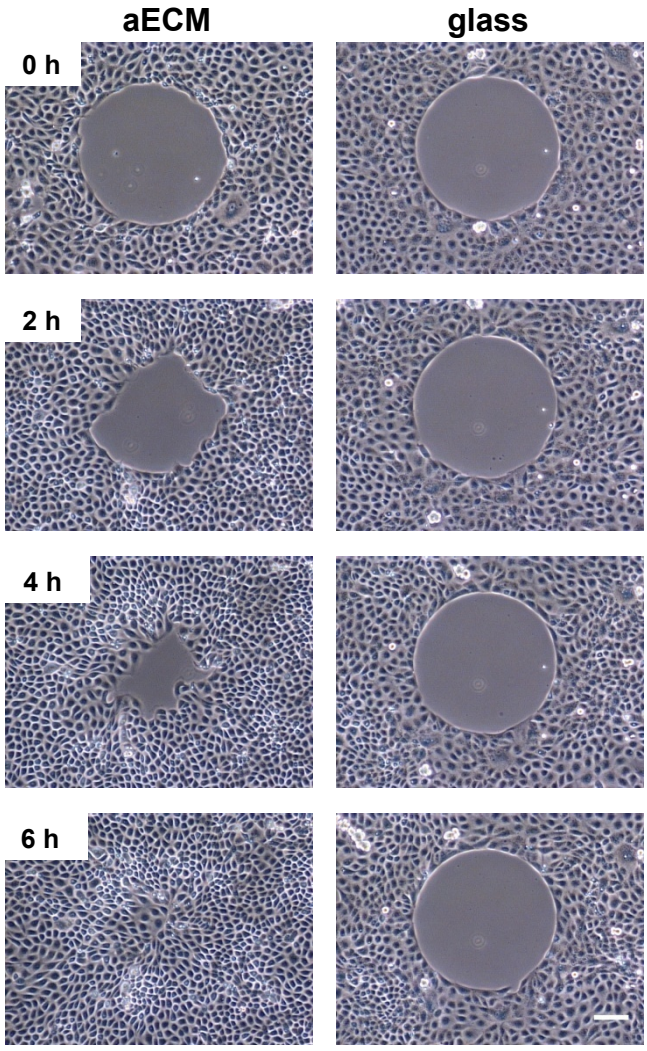

Figure 4.5 Time-lapse images of MDCK wound healing behavior on both aECM and untreated glass substrates. Time-lapse images show MDCK wound closure behavior on aECM (left panel) and on untreated glass (right panel) for a 400-μm-diameter circular wound. Scale bar represents 100 μm for all images.

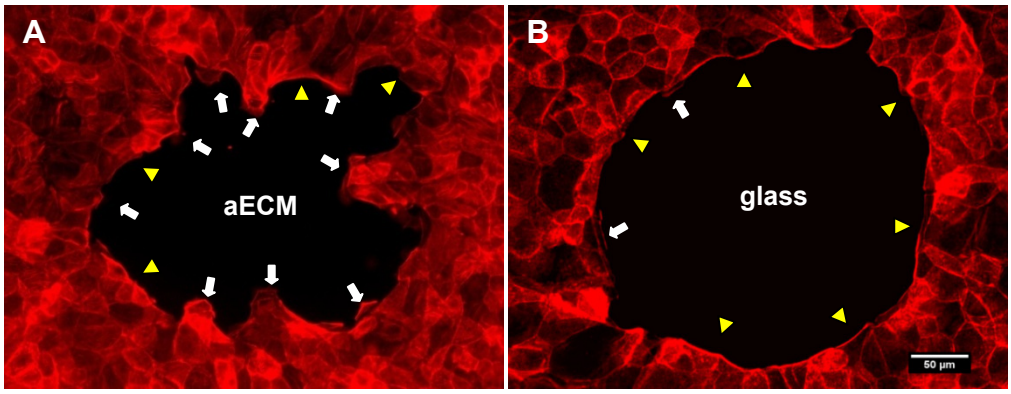

Figure 4.6 Verification of leader cells and purse-string structures. MDCK monolayers were wounded as described and allowed to heal on (**A**) aECM and (**B**) glass surfaces for 4 h. Cells were fixed and stained with phalloidin-rhodamine. White arrows indicate leader groups while yellow triangles indicate purse string structures. Scale bar represents 50 µm.

In the absence of ECM (i.e., on glass substrates), wound closure appeared to proceed largely by actomyosin contraction. The wound healing behavior was significantly slower and often led to incomplete wound closure even after 24 h (Fig 4.5, right panel). F-actin staining at 4 h after wounding confirmed the presence of actomyosin purse strings (yellow arrows) in these wounds (Figure 4.6B).

When we quantified the wound healing behaviors using MATLAB, we found that the number of leader cells increased with wound size on aECM surfaces but not on glass surfaces (Figure 4.7A). Although we observed one or two leader cells that developed spontaneously on glass, they moved with little persistence and retracted quickly (which accounted for the non-zero values for glass). The average spacing between consecutive leader groups, (L) was approximately 300 µm on aECM surfaces, independent of wound size (Figure 4.7B). Since no leader groups formed on glass surfaces, the spacing between

leader groups on glass was the entire length of the wound circumference (Figure 4.7B and inset).

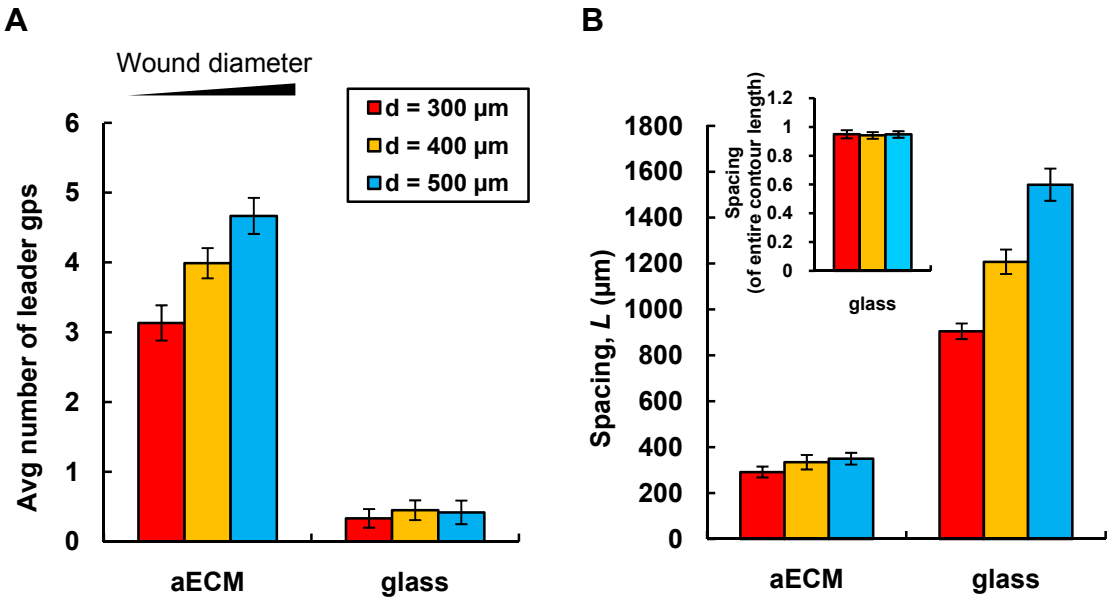

Figure 4.7 Quantification of wound healing behavior for circular wounds of increasing diameters. (**A**) The average number of leader groups as a function of wound size for aECM and glass. (**B**) The average spacing between these leader groups as a function of wound size. Inset represents the same data for glass as a fraction of total wound length. Error bars represent SEM.

To see if the spacing between leader cells was affected by decreasing the myosin II activity, we incubated wounded MDCK monolayers with blebbistatin, a known myosin II inhibitor (*15*). In blebbistatin-treated cultures, leader cells developed on glass substrates, resulting in patterns similar to those observed on aECM surfaces (Figure 4.8A). The average spacing between leader groups decreased with increasing blebbistatin concentrations (Figure 4.8B).

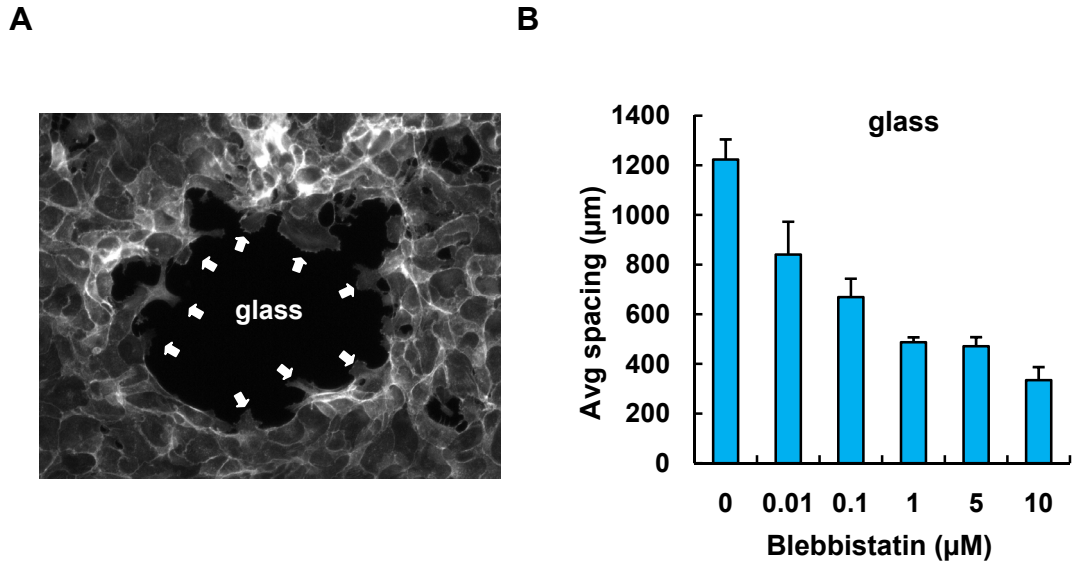

Figure 4.8 Effect of myosin inhibition on leader cell formation. (**A**) Wounded cell sheets were incubated in 5 μM blebbistatin and allowed to migrate over glass substrates. Cells were fixed and stained for F-actin. Arrows indicate leader groups. (**B**) The average spacing between leader groups decreases with increasing blebbistatin concentration. Error bars represent SEM.

From our experimental results, the selection of wound healing mechanism is dictated primarily by the presence of ECM in the wound area. The MDCK wound healing patterns observed on the aECM surfaces could be explained by a simple mechanical model. Figure 4.9 shows a schematic diagram of the proposed model. In the presence of ECM, leader cells develop at the wound edge and start to migrate into the wound. As they do so, they generate traction forces underneath the cell sheet (*10*). These forces are transmitted to neighboring cells through the adjacent actomyosin cable using the efficiency of myosin binding and unbinding (*16-17*). The increased tension inhibits the formation of additional leader cells in this region, resulting in regular spacing (*L*) between consecutive leader cells (see Figure 4.7B).

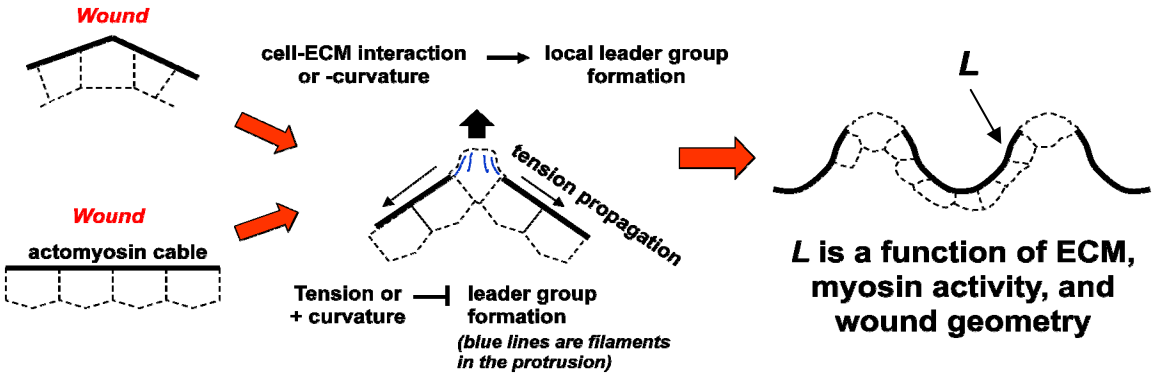

Figure 4.9 Schematic of proposed mechanical model. Model details and predictions can be found in the additional information section following this chapter.

The propagation of the tension through the actomyosin cables in our model depended on the activity of myosin II. Hence, increasing blebbistatin concentrations would increase the number leader cells formed (resulting in smaller spacing along the wound periphery). This argument is in line with our data obtained from the blebbistatin experiments (Figure 4.8). The model was further developed by Dr. Guo to yield predictions that were consistent with our experimental observations (see Figure B1 in the additional information for this chapter).

It is clear from our work and that of others (*15*), that cell-ECM interactions in the wound area provide the driving force for leader cell formation. Therefore, in the absence of ECM, cells rarely transform into leader cells. However, according to our model, we can also bias wound healing mechanisms by controlling wound geometry (Figure 4.9). To test this idea, we created zigzag-shaped wounds, and allowed MDCK cell monolayers to migrate on glass substrates. Indeed, 97.5% of the cells at apical regions ( ) of the zigzag wound adopted leader cell morphologies after 2.5 h, while only 4.7 % of the cells

at the concave ( ) regions became leaders (Figure 4.10A, B and E). Consequently, the leader cells also migrated on glass substrates even though cell-ECM interactions in the wound area were absent. This result is striking compared to a typical rectangular wound, where no leader cells were observed (and no advancement of the wound edge) was observed up to 24 h (Figure 4.10C, D and E).

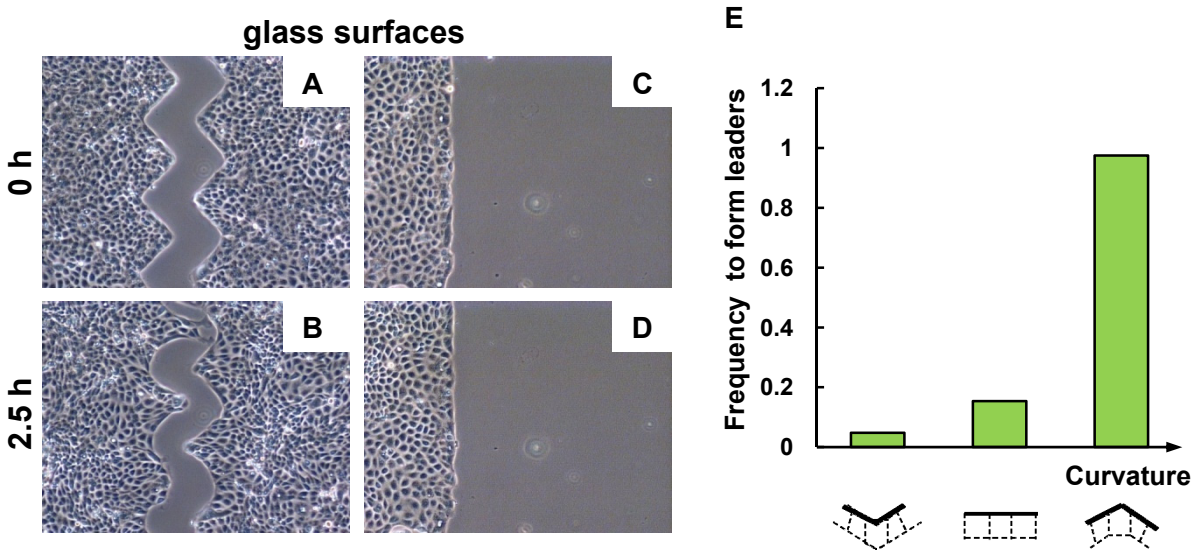

Figure 4.10 Wound curvature biases wound closure mechanisms. (**A – D**) show images of the wound edge at t = 0 h (**A, C**) and t = 2.5 h (**B, D**) migrating on glass substrates. Comparing (**B**) and (**D**), leader cells develop at apical regions ( ) whereas purse-strings form in all concave regions ( ) along the zig-zag wound edge. In contrast, in straight-edged wounds, no leader cell formation was observed up to 24 h. (**E**) The effect of wound curvature on the frequency of leader cell formation. The frequency to form leaders was obtained by dividing the total number of leader cells by the total number of convex, straight, or concave regions.

4.4 Conclusions

In this work, MDCK wound healing behavior was examined on both aECM and glass surfaces. We observed leader cell formation on aECM surfaces, while wounds close primarily via actomyosin purse strings on glass surfaces. Wound healing on aECM surfaces exhibited a characteristic healing pattern, which consists of successive leader cells separated by regions of actomyosin purse strings. The average spacing between consecutive leader cell groups was constant for wounds of increasing diameter. However, this spacing decreased with increasing myosin II inhibition. We proposed a simple phenomenological model to provide a qualitative explanation of the wound healing pattern in the presence of ECM. We also verified by experiments that the selection of healing mechanisms could be controlled by wound geometry.

4.5 Acknowledgements

I would like to acknowledge Dr. Carson Yu, Dr. Ouyang Mingxing, and Dr. Woonhee Lee for help with the CAD design of the micropatterned PDMS stamps. I also thank Dr. Woonhee Lee and Amy Lam for training on the clean room apparatus.

4.6 References

1. P. Martin, J. Lewis, *Nat. Lett.* **360**, 179 (1992).
2. W. M. Bement, P. Forscher, M. S. Mooseker, *J. Cell Biol.* **121**, 565 (1993).
3. D. P. Kiehart, *Curr. Biol.* **9**, R602 (1999).

4. M. Tamada, T. D. Perez, W. J. Nelson, M. P. Sheetz, *J. Cell Biol.* **176**, 27 (2007).

5. Y. Danjo, I. K. Gipson, *J. Cell Sci.* **111**, 3323 (1998).

6. A. Jacinto, A. Martinez-Arias, P. Martin, *Nat. Cell Biol.* **3**, E117 (2001).

7. R. Fernandez-Gonzalez, J. A. Zallen, *Sci. Signal.* **2**, pe78 (2009).

8. T. Omelchenko, J. M. Vasiliev, I. M. Gelfand, H. H. Feder, E. M. Bonder, *Proc. Natl. Acad. Sci. USA* **100**, 10788 (2003).

9. M. Poujade et al., *Proc. Natl. Acad. Sci. USA* **104**, 15988 (2007).

10. X. Trepat et al., *Nat. Phys. Lett.* **5**, 426 (2009).

11. G. Fenteany, P. A. Janmey, T. P. Stossel, *Curr. Biol.* **10**, 831 (2000).

12. J. C. MacDonald et al., *Electrophoresis* **21**, 27 (2000).

13. Y. Matsubayashi et al., *Curr. Biol.* **14**, 731 (2004).

14. D. L. Nikolić, A. N. Boettiger, D. Bar-Sagi, J. D. Carbeck, S. Y. Shvartsman, *Am. J. Physiol. Cell Physiol.* **291**, 68 (2006).

15. S. Grasso, J. A. Hernandez, S. Chifflet, *Am. J. Physiol. Cell Physiol.* **293**, C1327 (2007).

16. A. Vaezi, C. Bauer, V. Vasioukhin, E. Fuchs, *Dev. Cell* **3**, 367 (2002).

17. R. S. Fischer, M. Gardel, X. Ma, R. S. Adelstein, C. M. Waterman, *Curr. Biol.* **19**, 260 (2009).

ADDITIONAL INFORMATION FOR CHAPTER 4

The mathematical model (Work of Dr. Chin-lin Guo)

We used the following reasoning and assumptions to construct the model. We modeled the dynamics of filament density *f* at the adhesion site because both cell protrusion and adhesion formation depend on *f* (*1*), while *f* self-amplifies itself by using existing filaments as templates to nucleate more filaments (*2*). Meanwhile, we modeled the formation of actomyosin bundle *B* and the dynamics of its tension *T* because *T* down-regulates *f*, and the formation of *B* depends on *f* (*3*). The self-amplification of *f* is local, whereas myosin facilitates the transmission of *T* along the actomyosin bundle over the entire cell periphery. This tension is further transmitted between neighboring cells at the wound edge. As a result, we can model all the cells at the wound edge as a single entity and expect that the dynamics of *f* and *T* form a feedback circuit to control the shape of wound during the healing process. In this work, we used the change in *f* to indicate the corresponding change of cell shape in the formation of leader cells (i.e., a higher value of *f* corresponds to a higher propensity to form a cell protrusion).

First, we consider that at the wound edge, cells develop two profiles of filament density *f*: cell protrusion can occur above a certain threshold, and no cell protrusion forms below this threshold. Since the formation of an actomyosin bundle requires filaments polymerized at the adhesion sites, cells with a lower level of *f* possess a lower level of tension. However, the tension within these cells is increased if they are neighboring to cells that form protrusions (i.e., with a higher level of *f*), because the tension can be transmitted between neighboring cells and cells with a higher level of *f* produce a strong

tension. The increment of tension within the non-protruding cells further inhibits their formation of protrusions. As a result, we expected to see interleaved protruding and non-protruding cells along the wound edge. This leads to the pattern formation of two healing mechanisms.

To model *f* and *T*, we first set *N* discrete points along the edge of the wound. For each of these points, we assigned an index $i = 1$ to N with the $(i - 1)^{th}$ point next to the i^{th} point and the $(N + 1)^{th}$ point referred to the first point. For the dynamics of *f*, we first assumed that the rate of filament formation depends on *f* (*4*), the local curvature κ (*5*), and the density of adhesions *A* which is a function of *f* and the concentration of ECM molecules, [*ECM*] (*1*). Second, we assumed that the loss of *f* results from a tug-of-war between the tension from the actomyosin bundle, *T*, and the force generated by the motor clutch, F_{clutch}. Here we assumed that F_{clutch} depends on the myosin contractility *m*. We further assumed that the rate at which *f* decays is proportional to the ratio of *T* and F_{clutch}. In other words, a larger tension *T* results in a higher loss rate of *f*, whereas a stronger F_{clutch} allows for the accumulation of *f* and hence advances cell protrusion, Finally, we assumed that the accumulation of *f* at a point *i* increases its propensity to form a protrusion; this changes the membrane shape and in turn increases the chance to form more filaments at its neighboring points (*5*). Taken together, we have the equation for the dynamics of *f* at each point *i*, f_i,

$$\begin{aligned}\frac{df_i}{dt} &= k_{poly} e^{\kappa} f_i A_i - k_{diss} \frac{T_i}{F_{clutch}} f_i + D_m \left(f_{i+1} + f_{i-1} - 2f_i\right) \\ &= k_{poly} \frac{[ECM]}{K_d + [ECM]} e^{\kappa} f_i^2 - k_{diss} \frac{T_i}{m} f_i + D_m \left(f_{i+1} + f_{i-1} - 2f_i\right)\end{aligned} . \quad (3)$$

Here the first term indicates how adhesions and existing filaments f facilitate the polymerization of actin filaments, the second term indicates how the tug-of-war determines the rate of filament dissociation, and the third term indicates how the change of the membrane shape induced by neighboring points influences the filament formation with D_m as a coupling constant, where we approximated the shape effect by a term (f_{i+1} + f_{i-1} – $2f_i$) based on the assumption that the propensity to form a protrusion is proportional to f. In addition, we have used the approximation $A \sim f[ECM]/(K_d + [ECM])$ with K_d as the dissociation constant for ECM-integrin interaction, and used a term e^{κ} to mimic the curvature effect on the formation of actin filaments. In the present case, we found K_d is very small and the term $[ECM]/(K_d + [ECM])$ is saturated at even very low coating concentrations of ECM molecules. We set the rate at which f grows $\sim k_{poly} f e^{\kappa} A$ with k_{poly} as a constant. Likewise, we have approximated that $F_{clutch} \sim m$ and set the rate at which f decays $\sim k_{diss} T/F_{clutch}$ with k_{diss} as a constant.

For the dynamics of bundle tension T, we first assumed that the formation of the actomyosin bundle B depends on f and m, and the bundle generates the tension through a pairwise interaction. Second, we assumed that the dissembling of B and hence the dissipation of T depend on the curvature of the wound edge as well, in that curvatures that favor the formation of protrusions might enhance the dissembling of the actomyosin bundle (*5*). Third, we assumed that m facilitates the transmission of T between neighboring points (*3*). Taken together, we have the equation for the dynamics of T,

$$\begin{aligned} \frac{dT_i}{dt} &= k_T B_i^{\,2} - k_{dissip} e^{\kappa} T_i + m D_T \left[\left(T_{i+1} - T_i \right) + \left(T_{i-1} - T_i \right) \right] \\ &= k_T m^2 f_i^{\,2} - k_{dissip} e^{\kappa} T_i + m D_T \left(T_{i+1} + T_{i-1} - 2T_i \right) \end{aligned} . \qquad (4)$$

Here the first term indicates how myosin and existing filaments f facilitate the assembly of the bundle B which in turn generates the tension through a pairwise interaction, the second term indicates the dissipation of the tension at a rate of $k_{dissip}e^{\kappa}$ with k_{dissip} as a constant, and the third term indicates the transmission of the tension between neighboring points in a myosin-dependent manner with D_T as a constant. To obtain Equation 4, we have approximated $B \sim fm$ and set the rate at which T is created $\sim k_T B^2$ with k_T as a constant. Likewise, we have implemented myosin contractility m into the transmission efficiency of T between neighboring points. We did not express the tension T in a vector form because the directionality of the tension is balanced with intracellular pressure. For simplicity, the force balance within and between the cells were also ignored.

Next, we took the continuous limit by setting $N \rightarrow \infty$. We set l as the spacing between neighboring points and x as the coordinate along the periphery of a single cell or a single cell cluster. These allow us to rewrite Equations 3 and 4 to yield

$$\frac{df}{dt} = k_{poly}\frac{[ECM]}{K_d + [ECM]}e^{\kappa}f^2 - k_{diss}\frac{T}{m}f + D_m l^2\frac{d^2 f}{dx^2} \tag{5}$$

and

$$\frac{dT}{dt} = k_T m^2 f^2 - k_{dissip}e^{\kappa}T + mD_T l^2\frac{d^2 T}{dx^2}. \tag{6}$$

The continuous limit approach transformed our model into a reaction-diffusion scheme. Equations 5 and 6 were simplified by rescaling variables and grouping

parameters. By setting $u = (k_{diss}k_T m/k_{dissip}^2 e^{2\kappa} r[MLCK]_0)^{1/2} f$, $v = (k_{diss}/k_{dissip}e^{\kappa} m)T$, $\tau = k_{dissip}e^{\kappa}t$, $z = (k_{dissip}e^{\kappa}/D_m l^2)^{1/2}x$, $m' = mD_p/D_m$, and $\kappa' = \kappa + \frac{1}{2}\log(D_p/k_{diss}k_{poly}D_m)$, we have

$$\frac{du}{d\tau} = \alpha u^2 - vu + \frac{d^2u}{dz^2} \quad \text{, and} \tag{7}$$

$$\frac{dv}{d\tau} = u^2 - v + D\frac{d^2v}{dz^2} \quad , \tag{8}$$

where

$$\alpha = \frac{[ECM]}{K_d + [ECM]} \times \frac{e^{\kappa'}}{\sqrt{m'}}$$

as shown in Equation 1 is an effective "strength" to stimulate the accumulation of filaments and hence the formation of leader cell groups, and

$$D = m'$$

as shown in Equation 2 is an effective "diffusivity" to transmit the retraction tension and inhibit the formation of leader cells groups.

Model analysis

Equations 7 and 8 possess the same reaction-diffusion scheme as in the Turing model (*6*). Thus, we used the standard approach for Turing model (*6*) to obtain the analytical results. To proceed, we set $F(u, v) = \alpha u^2 - vu$ and $G(u, v) = u^2 - v$. According to reference (*6*), the system can form spatially inhomogeneous patterns only if a) in the

absence of diffusion there are at least one stable and non-zero steady-state solution, and b) in the presence of diffusion the stable steady-state solution becomes unstable, allowing the system to evolve from a spatially homogeneous state to a spatially inhomogeneous state, which in turn forms the morphological pattern. We examined the stability of the solution by performing the linear stability analysis; that is, allowing small perturbations of u and v away from their homogeneous steady-state solutions and using Fourier transform to identify the growth or decay rates of various modes parameterized by their wave number k. The mode with the dominant growth rate in turn determines the pattern (*6*).

We assumed (u_s, v_s) as the stable, non-zero, and spatially homogeneous steady-state solution in Equations 7 and 8. (u_s, v_s) satisfies $F(u_s, v_s) = G(u_s, v_s) = 0$, which leads to $u_s = \alpha$ and $v_s = \alpha^2$. To examine the stability of u_s and the corresponding pattern formation in Equations 7 and 8, we allowed small perturbations of u and v away from their homogeneous steady-state solutions, $u = u_s + \delta u$ and $v = v_s + \delta v$, and performed Fourier transform on δu and δv by setting $\delta u = \sum_{k=-\infty}^{\infty} A_k \exp(\lambda_k \tau + ikz)$ and $\delta v = \sum_{k=-\infty}^{\infty} B_k \exp(\lambda_k \tau + ikz)$, where k is the wave number, A_k and B_k are the magnitudes for each mode, λ_k is the growth or decay rate (depending on the sign), and $i = (-1)^{1/2}$ is the imaginary number. These lead to

$$\left(\lambda_k - F_u + k^2\right)A_k = F_v B_k \text{, and} \tag{9}$$

$$\left(\lambda_k - G_v + Dk^2\right)B_k = G_u A_k \text{,} \tag{10}$$

where

$$
\begin{aligned}
F_u &= \left.\frac{\partial F(u,v)}{\partial u}\right|_{u=u_s, v=v_s} = 2\alpha u_s - v_s = \alpha^2 \\
F_v &= \left.\frac{\partial F(u,v)}{\partial v}\right|_{u=u_s, v=v_s} = -u_s = -\alpha \\
G_u &= \left.\frac{\partial G(u,v)}{\partial u}\right|_{u=u_s, v=v_{ss}} = 2u_s = 2\alpha \\
G_v &= \left.\frac{\partial G(u,v)}{\partial v}\right|_{u=u_s, v=v_s} = -1
\end{aligned}
\quad . \tag{11}
$$

Multiplying Equations 9 and 10 from both sides to eliminate A_k and B_k (assuming that A_k and B_k both are non-zero), we have

$$
\lambda_k^2 + \left[(D+1)k^2 - (F_u + G_v)\right]\lambda_k + Dk^4 - (DF_u + G_v)k^2 + (F_u G_v - F_v G_u) = 0 . \tag{12}
$$

Equation 12 indicates that in the absence of diffusion term (i.e., $k = 0$), the steady-state solution (u_s, v_s) is stable only if there is no real and positive solution of λ_k; this requires $(F_u + G_v) < 0$ and $(F_u G_v - F_v G_u) > 0$, which requires $\alpha < 1$. Meanwhile, to have an unstable steady-state solution in the presence of diffusion, from Equation 12 we found that the term $Dk^4 - (DF_u + G_v)k^2 + (F_u G_v - F_v G_u) < 0$ is necessary, which occurs only if $(DF_u + G_v) \geq 0$ and $(DF_u + G_v)^2 \geq 4D(F_u G_v - F_v G_u)$. Taken together, these requirements confine a region in the parameter space,

$$
\frac{\sqrt{2}+1}{\sqrt{D}} \leq \alpha < 1 \tag{13}
$$

where cells or cell clusters can form non-random and non-uniform patterns.

From Equations 1 and 2, $\alpha = e^{\kappa'}[ECM]/m'^{1/2}(K_d + [ECM])$ and $D = m'$. Thus, Equation 13 indicates the range of the wound curvature and ECM molecule coating concentrations for the pattern formation of alternative healing mechanisms around the wound edge at a given myosin contractility m'. Inside the confined region the wound edge can form patterns. Outside the region, the healing is completely controlled by either the purse-string or leader cells. With these requirements, we can obtain the modes with real and positive λ_k, among which the dominant mode (i.e., the mode with largest growth rate) is the one satisfying $\partial\lambda_k / \partial k = 0$. From Equation 12, the wave number of the dominant mode, k_{dom}, obeys

$$D\left[(D-1)k_{dom}^2 + F_u - G_v\right]^2 + (D+1)^2 F_v G_u = 0 . \tag{14}$$

The mode of the dominant pattern can be expressed as $k_{dom} = 2n\pi/Z$ where n is an integer and Z is the periphery length of the wound. Thus, n defines the number of leader cell groups. For example, $n = 2$ represents the case where there are two separated leader cell groups along the wound edge.

Using Equation 11 and the relation $D = m'$, we rewrote Equation 14 for the mode with a wave number $k = 2n\pi/Z$ (n indicates the number of leader cell groups) as

$$n^2 = \left(\frac{Z}{2\pi}\right)^2 \frac{(m'+1)\sqrt{\frac{2}{m'}}\alpha - \alpha^2 - 1}{m'-1} . \tag{15}$$

Thus, for a given n, we can solve α numerically. Using graphical method, we found that smaller α leads to smaller n in Equation 15. For a fixed size of wound, this suggests that the absence of ECM molecules leads to a larger spacing between leader cell groups

(Figure B1a). At the same time, Equation 15 suggests that a smaller myosin contractility *m*' leads to a larger *n* (Figure B1b).

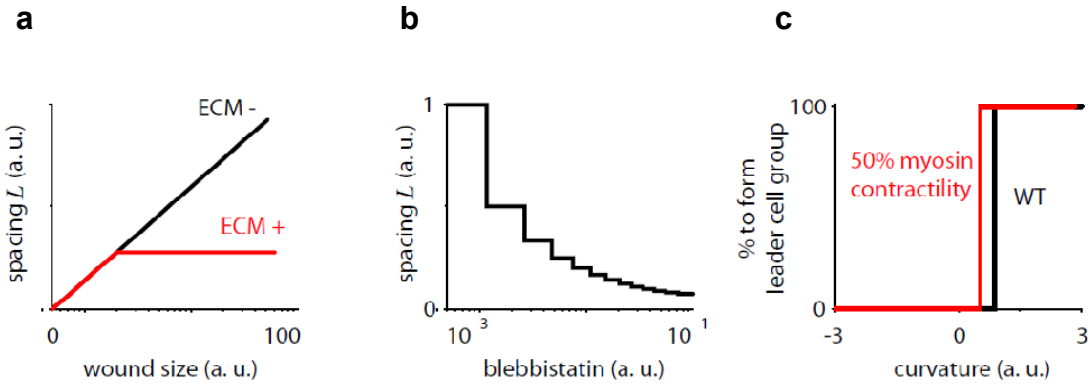

Figure B1 Model predictions. (**a**) The average spacing, *L* between consecutive leader cell groups as a function of wound size in the presence and absence of ECM. (**b**) The average spacing, *L* between leader cell groups as a function of increasing blebbistatin concentration. (**c**) Percent leader cell group formation as a function of wound curvature.

Parameters in Figure B1

To obtain Figure B1, we used the following parameters. For the change of spacing upon the treatment of blebbistatin, we set $(2\pi/Z)^2 = 0.003$ in Equation 15, the dose of blebbistatin = $1/m$', and $[ECM]e^{\kappa}/(K_d + [ECM]) = 8$ in Equation 1. We also used the reverse of *n*, $1/n$, to represent the spacing in Figure B1. To obtain the propensity of leader cell group formation on the change of the curvature, we identified the minimal α in Equation 1 which allows for an unstable non-zero steady-state solution in the absence of

diffusion term. This occurs at $\alpha = 1$ as shown in Equation 13. Then, we set $[ECM]/[(K_d + [ECM])(m')^{1/2}] = 1$ in Equation 1 to obtain the corresponding κ'.

References

1. M. Bailly, *Trends Cell Biol.* **13**, 163 (2003).

2. A. Upadhyaya, A. van Oudenaarden, *Curr. Biol.* **14**, R467 (2004).

3. A. Vaezi, C. Bauer, V. Vasioukhin, E. Fuchs, *Dev. Cell* **3**, 367 (2002).

4. L. G. Smith, R. Li, *Curr. Biol.* **14**, R109 (2004).

5. A. P. Liu et al., *Nat. Phys. Lett.* **4**, 789 (2008).

6. J. D. Murray, *Mathematical Biology*. S. A. Levin, Ed., Biomathematics, vol. 19, (Springer, New York, second ed., 1991), pp. 372 – 424.